Amine-functionalized metal–organic framework integrated bismuth tungstate (Bi$_2$WO$_6$/NH$_2$-UiO-66) composites for the enhanced solar-driven photocatalytic degradation of ciprofloxacin molecules[†]

> (i) Author and affiliation details can be edited in the panel that appears to the right when you click on the author list.

K. Rokesh Karuppannan, (0000-0001-7108-9813)[a], M. Sakar Mohan[a,b] and Trong-On Do, (0000-0002-7785-5299)[a,*]

[a]Department of Chemical Engineering, Laval University, Quebec, QC, , Canada, Trong-On.Do@gch.ulaval.ca

[b]Centre for Nano and Material Sciences, Jain University, Bangalore, 562112, Karnataka, India

Funding Information

Table of Contents Entry

An amine-functionalized metal–organic framework integrated bismuth tungstate (Bi$_2$WO$_6$/NH$_2$-UiO-66) nanocomposite has been developed *via* a hydrothermal technique and its photocatalytic performance towards ciprofloxacin degradation has been studied. The Bi$_2$WO$_6$/NH$_2$-UiO-66 composite with Z-Scheme heterojunction formation offered efficient charge separation and strong redox property towards ciprofloxacin degradation under solar light irradiation.

Abstract

An amine-functionalized metal–organic framework integrated bismuth tungstate (Bi$_2$WO$_6$/NH$_2$-UiO-66) nanocomposite has been developed by the *in situ* growth of NH$_2$-UiO-66 on Bi$_2$WO$_6$ micro/nanoflowers *via* a hydrothermal technique and its photocatalytic performance towards ciprofloxacin degradation under solar light irradiation has been studied. The integration of NH$_2$-UiO-66 with Bi$_2$WO$_6$ micro/nanoflowers extends its absorption-

edge towards the visible light region (∼470 nm) and the specific surface area of the Bi_2WO_6/NH_2-UiO-66 composite is estimated to be 113.6 m^2 g^{-1}. It is observed that the amine linkage established a strong interfacial contact between the NH_2-UiO-66 and Bi_2WO_6 micro/nanoflowers and formed a Z-scheme heterojunction in the composite. The Z-scheme heterojunction is found to lead to the effective photo-induced electron–hole pair separation and charge transfer kinetics, as well as providing strong oxidation and reduction sites in the composites, which leads to the degradation of around 83.1% of ciprofloxacin in 60 min. In addition, the h^+ and $O_2{}^{\cdot-}$ radicals are identified as major reactive species responsible for the photocatalytic process in the Bi_2WO_6/NH_2-UiO-66 composite, and thereby a possible photocatalytic mechanism is also proposed.

1. Introduction

The rising occurrence of pharmaceutical compounds in global water sources has resulted in emerging concerns because of their specific environmental risks and potential impact on ecosystems and human health.[1,2] Among them, antibiotics have become a growing concern due to the possible threat of the generation of antibiotic resistance in microorganisms and genotoxic effects. The antibiotic residues generate stable organic by-products, which leads to the formation of secondary pollutants, and they could produce serious toxicity and long-term chronic effects on humans and aquatic species and, hence, they are considered to be emerging pharmaceutical contaminants.[3–5] Consequently, there is an urgent need to find an efficient technique for the careful removal of new antibiotic pollutants from the water system. There are numerous techniques available to remove antibiotic residues from water, which include adsorption, microbial degradation, photocatalysis, ozonolysis, electrocatalysis and membrane filtration.[6–9] Among these techniques, semiconductor-based solar photocatalysts have been found to be of great interest because of their strong redox property, offering a high degradation efficiency and non-toxic by-product generation.[10,11] In particular, hybrid nanocomposite photocatalytic materials have been found to show higher antibiotic degradation efficiency. These hybrid photocatalysts are found to have suitable characteristic properties, such as superior structural, interface and surface properties, and thereby, the photo-absorbance, charge separation and transfer, redox ability and photostability of these systems is enhanced.[12–14]

Recently, a wide range of bismuth-based materials have been developed and studied for photocatalytic antibiotic degradation.[15–19] Of these materials, the layer-structured bismuth tungstate (Bi_2WO_6) materials have been found to be of great interest in the field of photocatalysis due to their visible light driven bandgap energy (2.7 eV), structural tunability, chemical stability, and non-toxicity. However, their practical application towards photocatalytic processes is limited by their low specific surface area, high electron–hole recombination, slow charge transfer and weak hydrophilicity.[20–23] To overcome these limitations, coupling Bi_2WO_6 with other semiconductors to construct hybrid composites could be an efficient way to achieve the desired high photocatalytic performance. This hybrid structure essentially offers favorable band structure alignments and efficient interfacial contacts in the system. Therefore, considerable efforts have been made to improve the charge carrier separation efficiency by constructing Bi_2WO_6 nanostructure-based heterojunctions with other semiconductors.[24,25]

In this direction, it has emerged that the incorporation of metal–organic frameworks (MOFs) with Bi_2WO_6 could be an efficient way to overcome the above limitations, including the high charge recombination, and to offer efficient charge separation and achieve fast transfer rates in the system.[26,27] MOFs are porous crystalline materials linked by organic ligands with transition metals and possess unique properties, such as a tunable porous structure, high ability to design them, high surface area, and strong adsorption ability.[28] Among them, UiO-66 is one of the most widely studied zirconium-based MOFs for photocatalytic applications owing to its large surface area, visible light absorbance, and relatively high structural stability in aqueous systems. However, the photocatalytic efficiency of UiO-66 is still limited due to its low charge separation, conductivity, and photo-activity. It is found that while introducing amino functional groups into UiO-66 extends the photo-absorption range in the visible region, it possibly provides a strong connection between the interfaces of composite counterparts, and thereby it is an efficient way to improve the charge separation and migration of photogenerated charge carriers and to increase the stability of composites.[29,30] Therefore, the incorporation of amine-functionalized UiO-66 (NH_2-UiO-66) with Bi_2WO_6 materials can provide efficient pathways for charge migration, leading to efficient photo-induced charge carrier separation in the system. In addition, the combination of these materials may lead to the establishment of a Z-scheme charge transfer mechanism and thus it will

enhance the overall redox potential of the composite, which will eventually be beneficial towards achieving improved photocatalytic efficiency. In this context, herein, we have developed a hybrid system based on NH_2-UiO-66 integrated Bi_2WO_6 *via* a two-step hydrothermal technique. The incorporation of NH_2-UiO-66 in Bi_2WO_6 micro/nanoflowers is found to potentially enhance the overall visible light absorbance of the composite and improve the charge separation and transfer efficiency in the system. Hence, the Bi_2WO_6/NH_2-UiO-66 composite exhibited a significantly higher photocatalytic activity towards antibiotic degradation under solar light irradiation.

2. Materials and methods

2.1 Chemicals

The chemicals, including bismuth nitrate pentahydrate $(Bi(NO_3)_3 \cdot 5H_2O)$, sodium tungstate dihydrate $(Na_2WO_4 \cdot 2H_2O)$, cetrimonium bromide (CTAB, $C_{19}H_{42}BrN$), zirconium tetrachloride $(ZrCl_4)$, terephthalic acid $(C_8H_6O_4)$, 2-aminoterephthalic acid $(C_8H_7NO_4)$ and *N,N*-dimethylformamide (DMF, C_3H_7NO) were obtained from Sigma Aldrich and used without any further purification.

2.2 Materials preparation

(i) Preparation of Bi_2WO_6 micro/nanoflowers

In a typical procedure, 2 mmol (0.97 g) of $Bi(NO_3)_3 \cdot 5H_2O$, 1 mmol (0.33 g) of $Na_2WO_4 \cdot 2H_2O$ and 0.05 g of CTAB were added to 80 mL of deionized water. After 30 min of stirring, the reaction mixture was transferred into a 140 mL Teflon-lined autoclave, which was sealed and heated at 120 °C for 24 h. The autoclave was naturally cooled to room temperature and the obtained final product was washed with deionized water and ethanol, followed by drying at 80 °C for 10 h (Scheme 1).

Scheme 1

Synthesis process of bare-Bi_2WO_6, Bi_2WO_6/UiO-66 and Bi_2WO_6/NH_2-UiO-66 composites *via* a two-step hydrothermal technique.
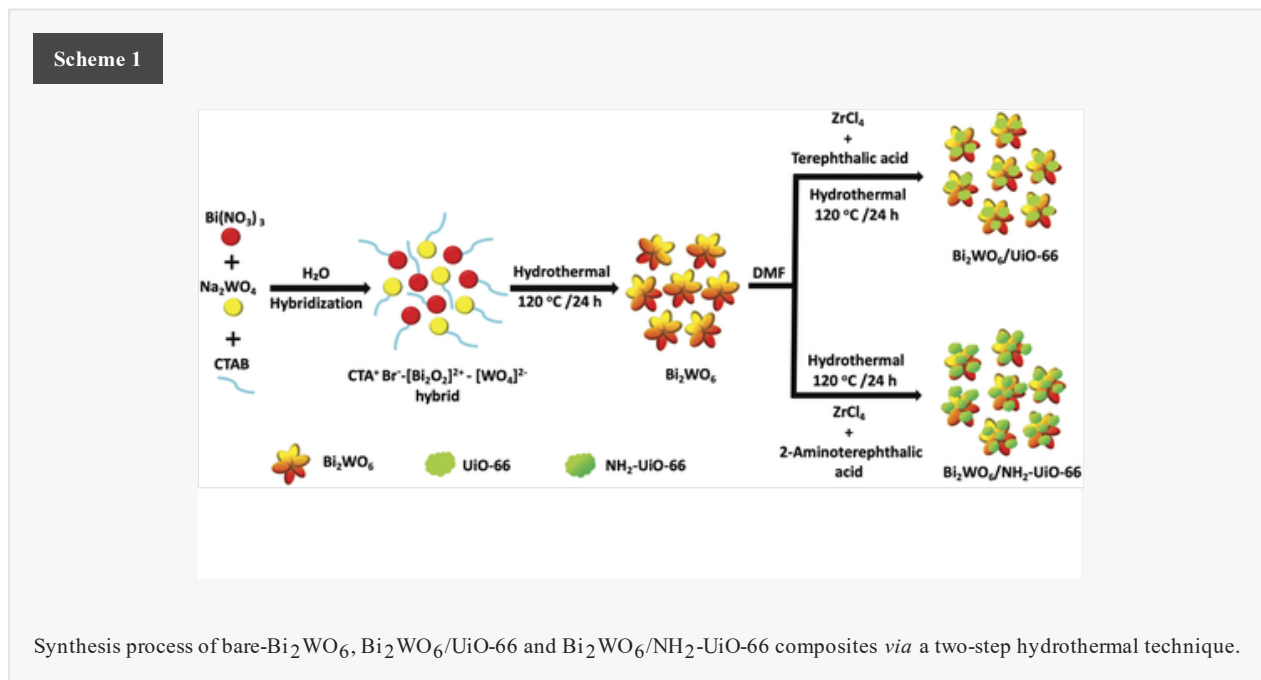
(ii) Preparation of Bi_2WO_6/UiO-66 and Bi_2WO_6/NH_2-UiO-66 composites

In this procedure, 0.25 g of the synthesized Bi_2WO_6 micro/nanoflowers was dispersed into 20 mL of DMF solution and sonicated for 30 min. Then, 0.025 g of $ZrCl_4$ in 20 mL of DMF solution was added to the above solution and stirred for 30 min. Subsequently, 0.05 g of terephthalic acid or 2-aminoterephthalic acid was dissolved in 20 mL of DMF solution and added into the above mixture and stirred for 30 min. Afterwards, the reaction mixture was transferred into a 140 mL Teflon-lined autoclave, which was sealed and heated at 120 °C for 24 h. The final obtained products were washed with ethanol several times and then heated in an oven at 80 °C overnight (Scheme 1).

2.3 Characterizations

The optical properties were studied using UV–visible spectroscopy (Cary 300 Bio UV–visible spectrophotometer). The crystalline nature of the materials was studied using the X-ray diffraction technique (Bruker SMART APEX II X-ray diffractometer equipped with a Cu Kα radiation source, $\lambda = 1.5418$ Å). Chemical functional groups were identified

using Fourier transform infrared spectroscopy (FTS 45 infrared spectrophotometer) with the KBr pellet technique. The morphology and structure of the materials were analyzed by scanning electron microscopy (FEI Inspect F50) and transmission electron microscopy (JEOL JEM 1230 instrument operated at 120 kV). The elemental compositions were identified by energy-dispersive X-ray spectroscopy (Edax Ametek Octane Super-A). The surface area was measured by the nitrogen adsorption–desorption isotherm technique using a Brunauer–Emmett–Teller instrument (Quantachrome Autosorb-1 MP analyzer). Emission spectra were obtained using a photoluminescence spectrometer (HORIBA PTI Quanta Master 500 spectrofluorometer) at an excitation wavelength of 380 nm. The photoelectrochemical properties were studied using a photo-electrochemical analyzer (Autolab PGSTAT 204) using a 100 W xenon arc lamp.

2.4 Photocatalytic experiment

The photocatalytic performance of the synthesized materials was examined for the degradation of the antibiotic ciprofloxacin under solar irradiation. In a typical experiment, 25 mg of the photocatalyst was suspended in 100 mL of ciprofloxacin (10 ppm) solution. A 100 W xenon arc lamp with a wavelength range of 250–1800 nm was used as the light source (ABET Sunlite solar simulator). Before the reaction, the photocatalyst–pollutant solution mixture was stirred in the dark for 15 min to establish the adsorption–desorption equilibrium, and later the suspension was kept under continuous light exposure for the degradation. Every 10 min, a small amount of the reaction solution was collected and centrifuged and the optical absorbance intensity was monitored using a UV–vis absorption spectrometer (UV–vis, Cary 300 Bio UV–visible spectrophotometer), which could be directly correlated to the amount of antibiotics degraded.

3. Result and discussion

3.1 Optical properties

The UV–visible diffuse reflectance spectra (UV–vis–DRS) of the synthesized bare-Bi_2WO_6, Bi_2WO_6/UiO-66 and Bi_2WO_6/NH_2-UiO-66 composites are presented in Fig. 1(a). In comparison with bare-Bi_2WO_6, the absorption band edges of the Bi_2WO_6/UiO-66 and Bi_2WO_6/NH_2-UiO-66 composites were blue and red-shifted, respectively. Notably, UiO-66 is typically UV-light active, whereas the amine–functionalized UiO-66 exhibits UV–visible light absorbance due to the $-NH_2$ groups that offer ligand-to-metal charge transfer. Therefore, the incorporation of UiO-66 shifted the overall photoabsorbance of the Bi_2WO_6/UiO-66 composites towards the UV region and NH_2-UiO-66 extended the photoabsorbance of Bi_2WO_6/NH_2-UiO-66 towards the visible light region.[31–33] Hence, the existence of amine groups in MOFs (*i.e.* NH_2-UiO-66) and their effective interface interaction with Bi_2WO_6 could form a strong heterostructure with a broad spectral response range in the visible light region.[30] Furthermore, the band gap energies of bare-Bi_2WO_6 and the Bi_2WO_6/UiO-66 and Bi_2WO_6/NH_2-UiO-66 composites were estimated using Tauc plots and were found to be 2.71, 2.79 and 2.58 eV, respectively, as shown in Fig. 1(b).[20,34,35] The band gap energy is found to be increased due to the incorporation of UiO-66 and it is decreased upon the incorporation of NH_2-UiO-66, due to which the Bi_2WO_6/NH_2-UiO-66 composite exhibited a relatively narrow band gap and extended absorbance in the visible light region.

Fig. 1

(a) UV–vis absorption spectra and (b) Tauc plot band gap energy estimation of bare-Bi_2WO_6 and the Bi_2WO_6/UiO-66 and Bi_2WO_6/NH_2-UiO-66 composites.
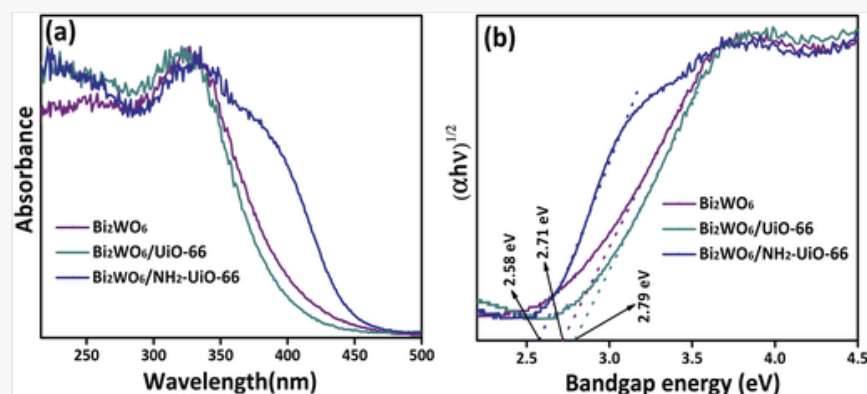
3.2 Structural and chemical composition

The X-ray diffraction (XRD) patterns of the synthesized bare-Bi_2WO_6 and the Bi_2WO_6/UiO-66 and Bi_2WO_6/NH_2-UiO-66 composites are shown in Fig. 2(a). The observed sharp diffraction peaks represent the excellent crystalline properties of the synthesized materials and the absence of peaks other than those of the parent material indicates the purity of the materials, which are free from impurities and/or secondary phases. Notably, the observed doublet peak corresponding to bare Bi_2WO_6 is merged in the case of the composites (as shown in Fig. S1(a) in the ESI[†]), which indicates that the integrated NH_2-UiO-66 MOF has a lattice level interaction with the host Bi_2WO_6 system. Furthermore, the obtained XRD patterns confirmed the orthorhombic structure of Bi_2WO_6 (JCPDS No. 73-2020).[36,37] and both the composites Bi_2WO_6/UiO-66 and Bi_2WO_6/NH_2-UiO-66 showed similar XRD patterns to those of Bi_2WO_6, and the peaks corresponding to UiO-66 and NH_2-UiO-66 were also identified in the XRD patterns of the respective composites. In addition, the XRD patterns of bare UiO-66 and NH_2-UiO-66 are also given in Fig. S1(b) in the ESI.[†] It should be noted that the peaks corresponding to Bi_2WO_6 were not found to be shifted upon the incorporation of UiO-66 and NH_2-UiO-66, which revealed that the integration of these MOFs did not influence the crystal structure of Bi_2WO_6. For the composites, the peaks at 7.25°, 23.31° and 25.74° correspond to UiO-66 and NH_2-UiO-66, but their peak intensities are relatively low due to their lower concentrations in the composites.[31,38] As compared to Bi_2WO_6/UiO-66, Bi_2WO_6/NH_2-UiO-66 showed a major intensity peak at 7.25°, which can be attributed to the existence of a stronger interaction between the $-NH_2$ groups in UiO-66 and Bi_2WO_6.[33] Furthermore, the obtained sharp diffraction peaks and absence of any other unknown peaks indicated the purity of the synthesized materials.

Fig. 2
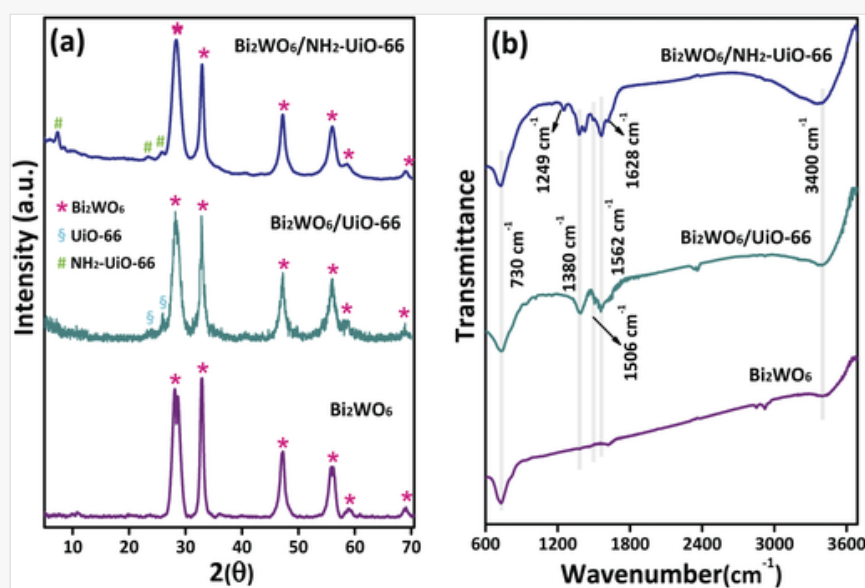
(a) X-ray diffraction and (b) FTIR spectra of bare-Bi_2WO_6 and the Bi_2WO_6/UiO-66 and Bi_2WO_6/NH_2-UiO-66 composites.

The existence of various chemical functional groups in the materials was confirmed using Fourier transform infrared spectroscopy (FTIR) analysis, as shown in Fig. 2(b). The characteristic peak obtained at 730 cm^{-1} corresponded to the W–O stretching vibration in the Bi_2WO_6 phase, while the vibration peaks of Bi_2WO_6/NH_2-UiO-66 were slightly shifted towards a higher wavenumber as compared to those of the Bi_2WO_6/UiO-66 composite, which could be due to the stronger interaction of NH_2-UiO-66 with Bi_2WO_6.[39] The composites Bi_2WO_6/UiO-66 and Bi_2WO_6/NH_2-UiO-66 displayed peaks at 1380 and 1562 cm^{-1}, which were related to the symmetric and asymmetric carboxylate (O–C$=$O) groups, respectively, of the UiO-66 and NH_2-UiO-66. The weak vibration at 1506 cm^{-1} was ascribed to the C$=$C of the benzene ring in the UiO-66 and NH_2-UiO-66.[32,40,41] In addition, the Bi_2WO_6/NH_2-UiO-66 composite displayed a peak at 1249 cm^{-1}, which could be assigned to the C–N stretching vibration of aromatic amines and the

peak at 1628 cm^{-1} represented the N–H bending vibration of NH$_2$-UiO-66. These results confirmed the presence of –NH$_2$ linkers in the composite, which were found to be prominent for the Bi$_2$WO$_6$/NH$_2$-UiO-66 composite due to the greater interaction at their interfaces.[30,42] The IR spectra also showed a peak at 3400 cm^{-1}, corresponding to the stretching vibration of the –OH group in the materials, whereas in the Bi$_2$WO$_6$/NH$_2$-UiO-66 composite, this vibration peak was relatively broad, which could be attributed to the N–H stretching in the composite.[30] These observations confirmed that there could be the formation of a Bi–W–O–N–C–O–Zr network in the system, which ultimately gave rise to the optical and electronic properties of the composite.

3.3 Morphology and surface analysis

The morphology and structure of the bare-Bi$_2$WO$_6$ and the Bi$_2$WO$_6$/UiO-66 and Bi$_2$WO$_6$/NH$_2$-UiO-66 composites were analysed using scanning electron microscopy (SEM) and transmission electron microscopy (TEM), as shown in Fig. 3(a)–(i). The developed bare-Bi$_2$WO$_6$ exhibited a flower-like morphology, which could be due to the assembly of small nanoflakes into micro/nanoflowers with diameters of around 4 to 5 μm (Fig. 3(a)–(c)).[25,43] The morphologies of the Bi$_2$WO$_6$/UiO-66 and Bi$_2$WO$_6$/NH$_2$-UiO-66 composites were significantly altered upon the integration of UiO-66 and NH$_2$-UiO-66 onto the Bi$_2$WO$_6$ surface, respectively, which considerably influenced the nano/micro flower surface, as shown in Fig. 3(e) and (h). Furthermore, SEM results revealed that the UiO-66 and NH$_2$-UiO-66 particles were aggregated with the Bi$_2$WO$_6$ micro/nanoflowers. However, as compared to UiO-66, the NH$_2$-UiO-66 significantly altered the morphology of the composite. This could be attributed to the –NH$_2$ functional groups, which possibly established a potential binding of NH$_2$-UiO-66 on the Bi$_2$WO$_6$ micro/nanoflower surface. Therefore, the increased amount of NH$_2$-UiO-66 on the Bi$_2$WO$_6$ surface strongly covered the microflower surface and transformed the microflowers into microparticles.[30,35,44] Both the SEM and TEM images confirmed that the NH$_2$-UiO-66 and Bi$_2$WO$_6$ were closely connected, which could be corroborated with the XRD and FTIR analysis as well. Furthermore, the elemental composition of the materials was confirmed by energy-dispersive X-ray spectroscopy (EDS), as shown in Fig. S2 (ESI†). The elements Zr, C and N were detected in the EDS spectrum of Bi$_2$WO$_6$/NH$_2$-UiO-66, which confirmed the presence of NH$_2$-UiO-66 in the composite.[45]

Fig. 3

SEM and TEM images of (a–c) bare-Bi$_2$WO$_6$, (d–f) the Bi$_2$WO$_6$/UiO-66 composite and (g–i) the Bi$_2$WO$_6$/NH$_2$-UiO-66 composite, and (j) nitrogen adsorption–desorption isotherm of bare-Bi$_2$WO$_6$ and the Bi$_2$WO$_6$/UiO-66 and Bi$_2$WO$_6$/NH$_2$-UiO-66 composites.
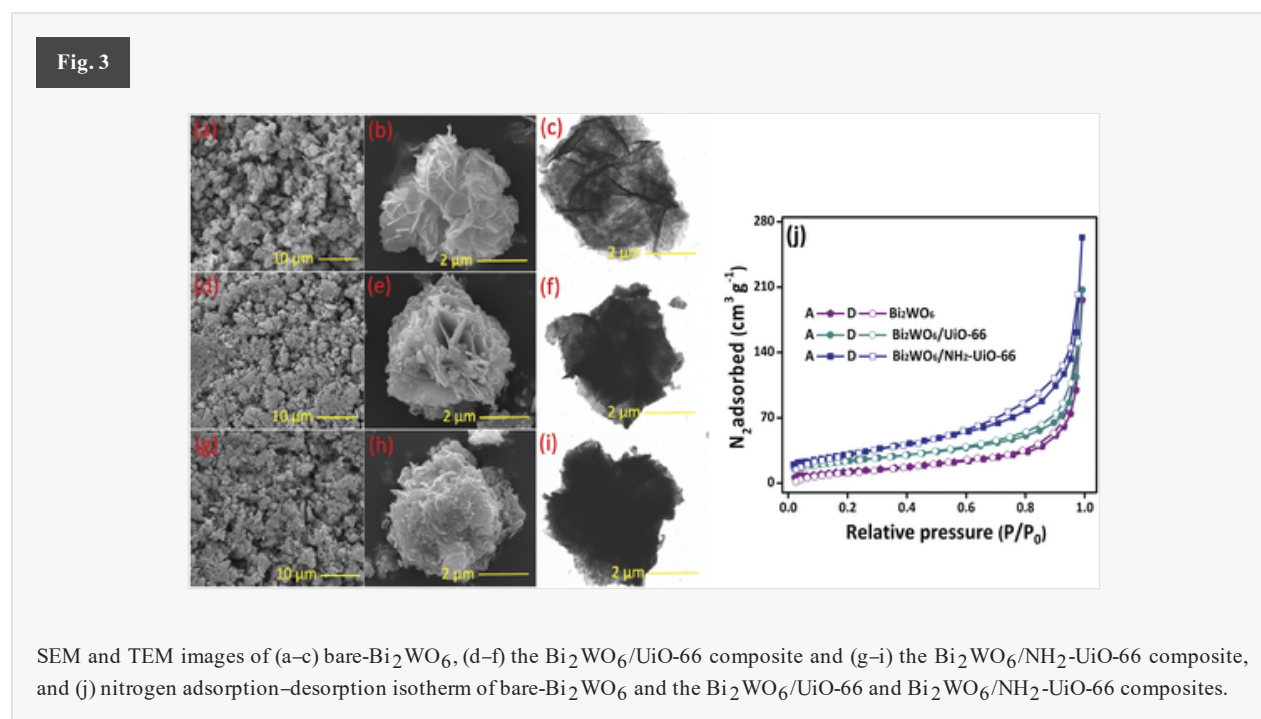
The specific surface areas of bare-Bi$_2$WO$_6$ and the Bi$_2$WO$_6$/UiO-66 and Bi$_2$WO$_6$/NH$_2$-UiO-66 composites were measured by Brunauer–Emmett–Teller (BET) analysis using nitrogen (N$_2$) adsorption–desorption measurements, as displayed in Fig. 3(j). The estimated surface areas of Bi$_2$WO$_6$, Bi$_2$WO$_6$/UiO-66 and Bi$_2$WO$_6$/NH$_2$-UiO-66 were around 47.9, 83.7 and 113.6 m^2 g^{-1}, respectively. It is clear that the incorporation of UiO-66 and NH$_2$-UiO-66 significantly improved the overall specific surface area of the Bi$_2$WO$_6$/UiO-66 and Bi$_2$WO$_6$/NH$_2$-UiO-66 composites and the observed increased surface area of Bi$_2$WO$_6$/NH$_2$-UiO-66 could be attributed to the –NH$_2$ groups, which established a stronger and stable integration of NH$_2$-UiO-66 on the surface of Bi$_2$WO$_6$, which also increased the quantity of NH$_2$-UiO-66 on the micro/nanoflower surface as well. Moreover, the absence of the amine linker in UiO-

66 meant that only electrostatic interactions could be established between UiO-66 and Bi_2WO_6 and thereby the overall surface area was reduced for the Bi_2WO_6/UiO-66 composite as compared to that of the other composite. Notably, the improved specific surface area could favor the generation of more active species and offer enhanced adsorption of more antibiotic molecules, and thereby it could contribute to the higher photocatalytic performance.[35,46]

3.4 Photoinduced charge separation and transfer characteristics

The photogenerated charge separation efficiencies of bare-Bi_2WO_6 and the Bi_2WO_6/UiO-66 and Bi_2WO_6/NH_2-UiO-66 composites were studied using photoluminescence (PL) analysis and the corresponding results are displayed in Fig. 4(a). As compared to bare-Bi_2WO_6, the Bi_2WO_6/UiO-66 and Bi_2WO_6/NH_2-UiO-66 composites showed reduced PL emission intensity, which indicated that the composites possessed lower recombination resistance and higher photoinduced electron–hole separation in the systems. This could be attributed to the formation of heterojunctions between Bi_2WO_6 and UiO-66/NH_2-UiO-66, resulting in the favorable band structure for the improved separation and transfer of photo-generated charge carriers within the composites, as well as to the reactant molecules. Furthermore, as revealed by the FTIR analysis, NH_2-UiO-66 was strongly incorporated onto the Bi_2WO_6 micro/nanoflowers and greatly facilitated the stronger interfacial contact between Bi_2WO_6 and NH_2-UiO-66; thus, the composite possessed an improved photo-generated charge carrier transfer rate through the formation of heterojunctions *via* the Bi–W–O–N–C–O–Zr network. Moreover, the Bi_2WO_6/NH_2-UiO-66 composite showed relatively enhanced charge separation and migration, which could be attributed to the amine functional group establishing a strong interfacial contact between the Bi_2WO_6 and NH_2-UiO-66 heterostructures.[31,44,45]

Fig. 4
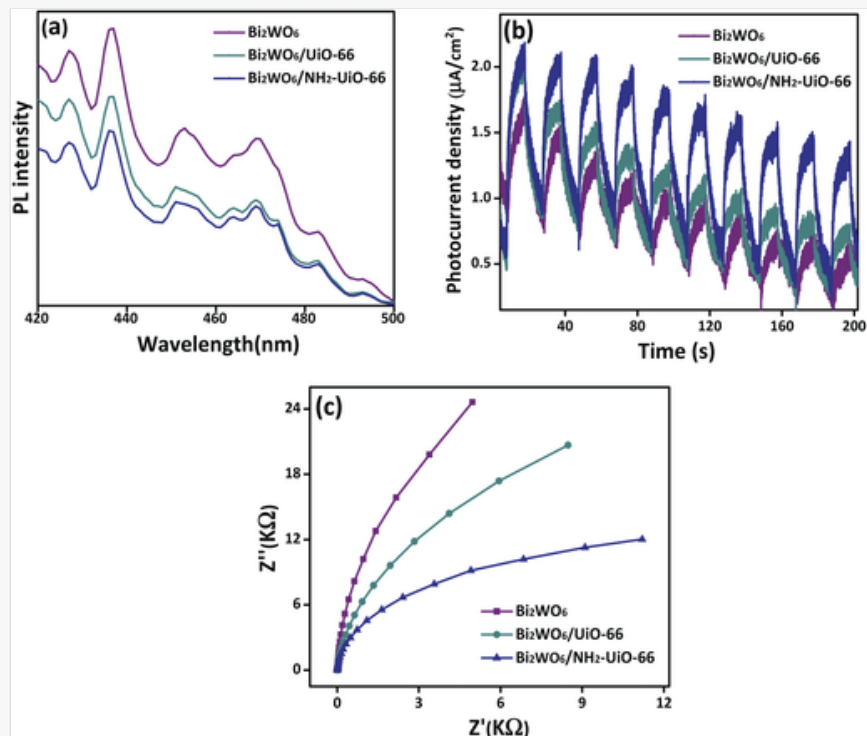
(a) Photoluminescence, (b) chronoamperometric and (c) Nyquist plots of bare-Bi_2WO_6 and the Bi_2WO_6/UiO-66 and Bi_2WO_6/NH_2-UiO-66 composites.

Furthermore, the photogenerated charge carrier separation and transfer efficiencies of the materials were measured by the photoelectrochemical (PEC) technique. The photocurrent generation in bare-Bi_2WO_6 and the Bi_2WO_6/UiO-66 and Bi_2WO_6/NH_2-UiO-66 composites were estimated by the chronoamperometry technique with a light "on--off" process under solar light irradiation (Fig. 4(b)). The developed materials showed good photocurrent generation, and the intensity of the photocurrent was increased during light irradiation and decreased to zero when the light irradiation was turned off. Upon comparison, the Bi_2WO_6/NH_2-UiO-66 composite showed a higher photocurrent generation efficiency and a high photocurrent density of around 1.42 $\mu A \ cm^{-2}$. The enhanced photocurrent generation could be attributed to the amine linker, resulting in efficient photocurrent conduction *via* the formed heterojunction along with a strong interfacial connection between Bi_2WO_6 and NH_2-UiO-66.[45,47] In addition, the Nyquist plots were obtained to analyze the charge transfer efficiency in the systems using the electrochemical impedance technique and the corresponding results are displayed in Fig. 4(c). The obtained results showed that the Bi_2WO_6/NH_2-UiO-66 composite exhibited a smaller arc radius that indicated the smaller charge transfer resistance in the system as compared to those of the Bi_2WO_6/UiO-66 and bare-Bi_2WO_6 materials. The lower resistance of Bi_2WO_6/NH_2-UiO-66 could be attributed to the establishment of conducting channels to facilitate the migration of photo-generated electrons from Bi_2WO_6 and NH_2-UiO-66 *via* the Bi−W−O−N−C−O−Zr network in the system. This eventually lowered the interface

resistivity and increased the fast charge transfer efficiency, along with offering a better photo-stability to the composite.[33,46]

3.5 Photocatalytic activity

The photocatalytic performances of bare-Bi_2WO_6 and the Bi_2WO_6/UiO-66 and Bi_2WO_6/NH_2-UiO-66 composites were studied toward the degradation of the antibiotic ciprofloxacin (CIP) under solar light irradiation and the obtained degradation results are shown in Fig. 5(a). The time-dependent optical degradation spectra of ciprofloxacin over Bi_2WO_6, Bi_2WO_6/UiO-66 and Bi_2WO_6/NH_2-UiO-66 are given in Fig. S3(a–c) in the ESI.[†] The materials showed photocatalytic activity towards ciprofloxacin degradation in the order of Bi_2WO_6/NH_2-UiO-66 > Bi_2WO_6/UiO-66 > Bi_2WO_6, with degradations of 83.1, 57.7 and 34.6%, respectively, after 60 min. Upon comparison, the Bi_2WO_6/NH_2-UiO-66 composite revealed a higher photocatalytic activity, and this was found to be around 2.4 and 1.45 fold higher than those of Bi_2WO_6 and Bi_2WO_6/UiO-66, respectively. The observed superior photocatalytic performance of Bi_2WO_6/NH_2-UiO-66 could be readily attributed to the improved photoinduced rate of charge carrier separation and transfer due to the formation of heterojunctions *via* the amine linkage. In addition, the extended photo-absorbance offered higher solar light absorption and the specific surface area provided a large number of reactive sites to the Bi_2WO_6/NH_2-UiO-66 composites, which contributed to improving the overall photocatalytic properties of the system. Furthermore, to investigate the key radical species responsible for the photocatalytic activity in the Bi_2WO_6/NH_2-UiO-66 composite, scavenging experiments using different scavenging agents, such as triethanolamine (TEOA), isopropyl alcohol (IPA) and *p*-benzoquinone (BQ), corresponding to h^+, $OH^{\cdot}$ and $O_2^{\cdot-}$ species, respectively, were carried out and the obtained results are displayed in Fig. 5(b).

Fig. 5

(a) Photocatalytic degradation of the antibiotic ciprofloxacin by bare-Bi_2WO_6 and the Bi_2WO_6/UiO-66 and Bi_2WO_6/NH_2-UiO-66 composites under solar light irradiation and (b) radical scavenger tests over the Bi_2WO_6/NH_2-UiO-66 composite.
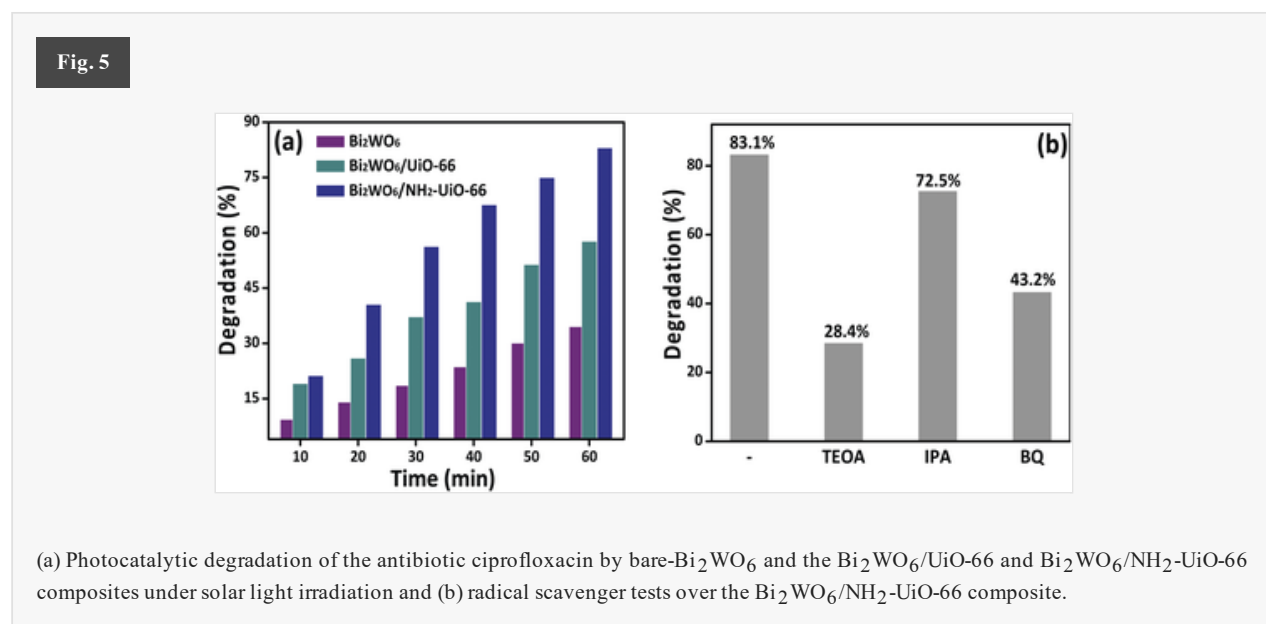
The results showed that the degradation efficiency dropped to 28.4, 72.5 and 43.5% in the presence of TEOA, IPA and BQ, respectively, whereas without scavengers the ciprofloxacin degradation was 83.1%. Therefore, it was confirmed that holes (h^+) and superoxide radicals ($O_2^{\cdot-}$) could be the main active species involved in the photocatalytic ciprofloxacin degradation process, rather than $OH^{\cdot}$ radicals.[48,49] The band structure of the photocatalysts is a key factor in determining the photocatalytic redox potential, as well as the photocatalytic efficiency of the heterojunction composites. Therefore, the band positions of Bi_2WO_6 (+2.69 eV VB and −0.02 eV CB), UiO-66 (+3.34 eV VB and −0.55 eV CB) and NH_2-UiO-66 (+2.30 eV VB and −0.35 eV CB) were estimated using Mott–Schottky plot[50,51] and Tauc plot[20,51] analysis and the corresponding results are given in Fig. 6(a)–(c) and 7(a)–(c), respectively.

Fig. 6
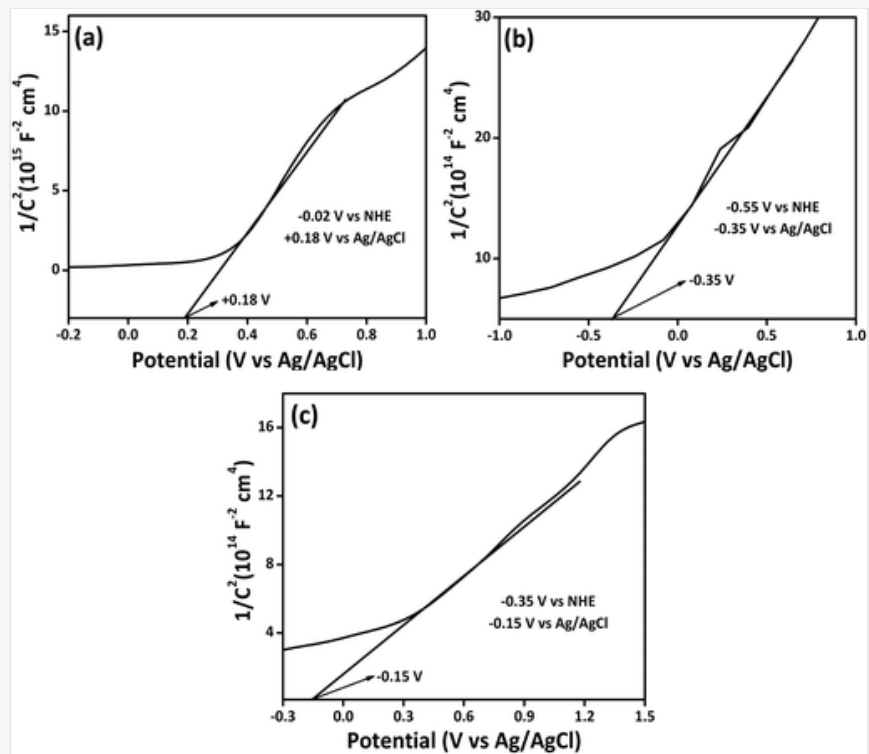
Mott–Schottky plots of (a) Bi_2WO_6, (b) UiO-66 and (c) NH_2-UiO-66.

Fig. 7
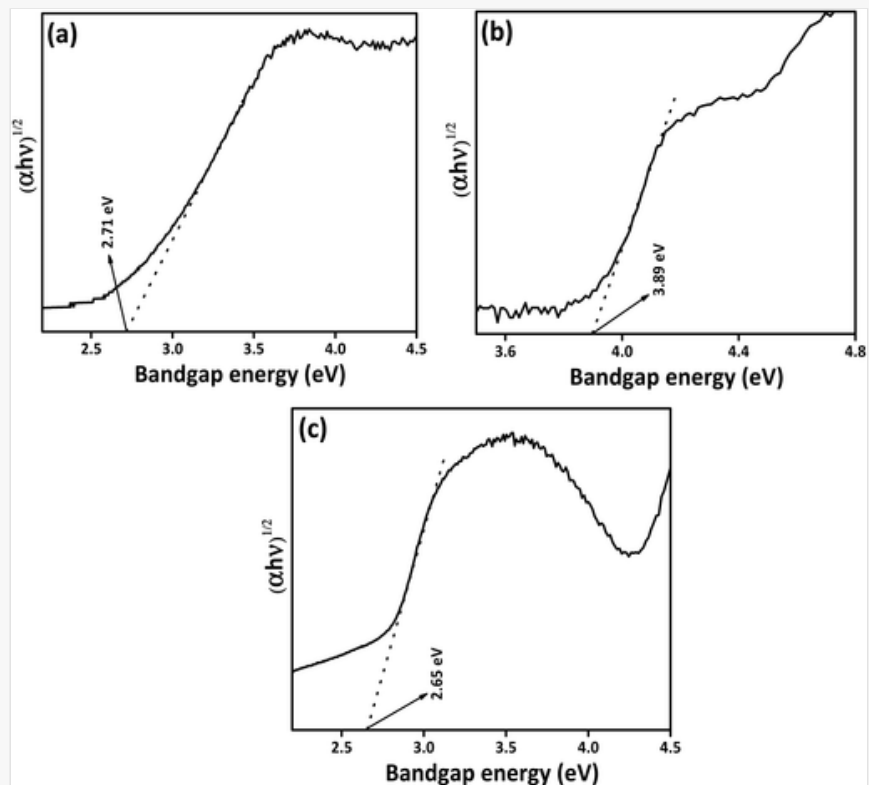
Tauc plots of (a) Bi_2WO_6, (b) UiO-66 and (c) NH_2-UiO-66.

Furthermore, the schematic illustrations shown in Fig. 8(a) and (b) represent the photocatalytic charge transfer mechanisms in the Bi_2WO_6/UiO-66 and Bi_2WO_6/NH_2-UiO-66 composites, respectively, towards the degradation of ciprofloxacin. It can be seen that the photo-generated electrons in Bi_2WO_6 undergo migration from the CB of Bi_2WO_6 to the VB of UiO-66 and NH_2-UiO-66; meanwhile, the electrons in the VB of UiO-66 and NH_2-UiO-66 also get excited to their respective CBs under solar light irradiation. Based on the band structure, the VB potential of Bi_2WO_6 (+2.69 eV) could be enough to generate hydroxyl radicals (OH˙/OH$^-$ = 1.99 eV), but the CB of Bi_2WO_6 (−0.02 eV) may not be enough to generate superoxide radicals (O_2/O_2˙$^-$ = −0.33 eV). Similarly, the VB (+3.34 eV) and CB (−0.55 eV) potentials of UiO-66 and the VB (+2.30 eV) and CB (−0.35 eV) potentials of NH_2-UiO-66 both are suitable to generate hydroxyl radicals (OH˙/OH$^-$ = 1.99 eV) and superoxide radicals (O_2/O_2˙$^-$ = −0.33 eV). However, the Bi_2WO_6/UiO-66 and Bi_2WO_6/NH_2-UiO-66 heterojunction composite led to the Z-scheme charge transfer mechanism with a strong redox property, and this can establish a strong oxidation ability at the valence band (VB) of Bi_2WO_6 and a high reduction ability at the conduction band (CB) of UiO-66 and NH_2-UiO-66. Therefore, the generated holes at the VB of Bi_2WO_6 are spontaneously involved in the direct oxidation of ciprofloxacin and/or oxidize the water molecules, and thereby the hydroxyl radicals involved in the oxidation mediated degradation of ciprofloxacin are generated. On other hand, the electrons at the CB of UiO-66 and NH_2-UiO-66 reduce the oxygen molecule and produce superoxide radicals, and thereby they are involved in ciprofloxacin degradation. Moreover, it is possible that the electrons excited to the CB of the Bi_2WO_6/UiO-66 composite may recombine relatively faster as compared to those in Bi_2WO_6/NH_2-UiO-66 due to the relative band edge potentials of the VB of UiO-66, as shown in Fig. 8(a). Hence, the integration of NH_2-UiO-66 with Bi_2WO_6 established a Z-scheme heterojunction with efficient

charge separation and high redox properties, which potentially led to the efficient degradation of ciprofloxacin molecules.[52–54]
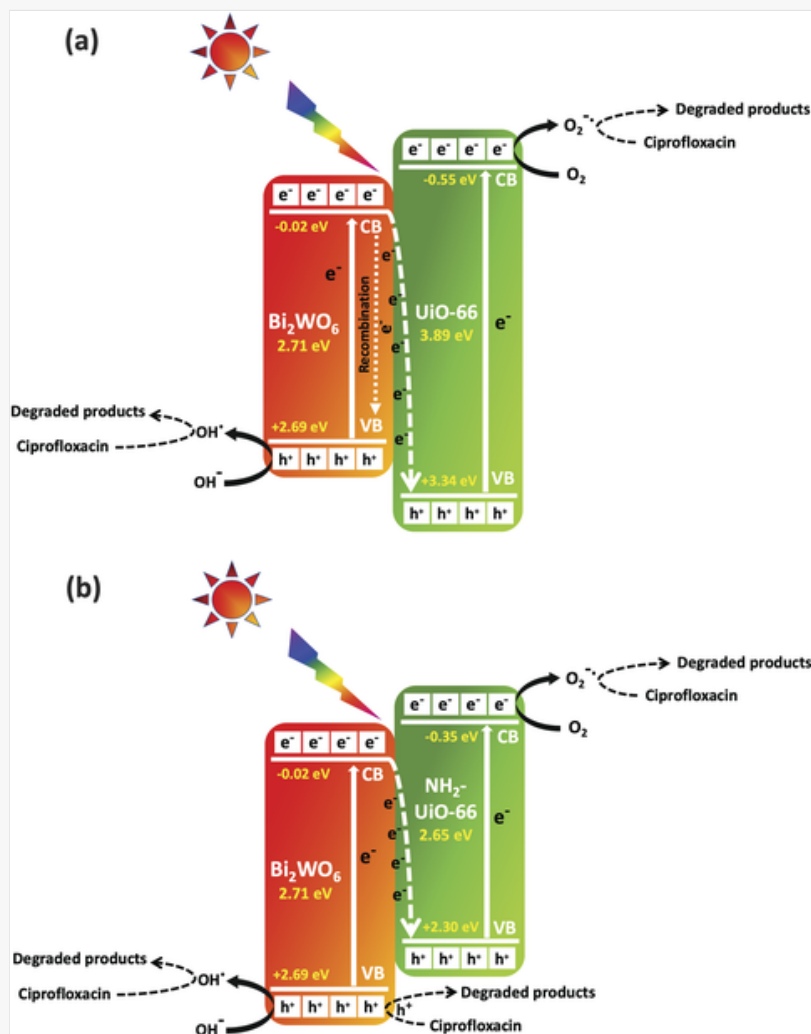
Fig. 8 Proposed Z-scheme charge transfer mediated photocatalytic degradation mechanism of the (a) Bi_2WO_6/UiO-66 and (b) Bi_2WO_6/NH_2-UiO-66 composites.

Furthermore, the stability of the photocatalyst was studied through the reusability experiments for up to five cycles using the Bi_2WO_6/UiO-66 and Bi_2WO_6/NH_2-UiO-66 photocatalysts under the same experimental conditions, and the obtained results are given in Fig. S4(a) and (b) (ESI†). The obtained results revealed that both of the composites showed better stability and consistency towards the photocatalytic degradation of CIP molecules. However, Bi_2WO_6/NH_2-UiO-66 showed a relatively higher recyclability across the entire five cycles as compared to that of Bi_2WO_6/UiO-66, and this could be mainly attributed to the stronger interfacial contact and stabilized structural properties established by the amine-functionalized UiO-66 MOFs.[30,51]

4. Conclusion

In this study, the development of a Bi_2WO_6/NH_2-UiO-66 nanocomposite by anchoring NH_2-UiO-66 on the Bi_2WO_6 micro/nanoflower surface, and its enhanced photocatalytic activity towards the degradation of molecules of the antibiotic ciprofloxacin under solar light irradiation, were demonstrated. The improved photocatalytic activity of the Bi_2WO_6/NH_2-UiO-66 composite was attributed to the formation of a heterojunction with strong interfacial contact between Bi_2WO_6 and NH_2-UiO-66 via a Bi–W–O–N–C–O–Zr network, which favored broadening the spectral response range, reduced the photogenerated electron–hole pair recombination, and increased the photogenerated charge transfer in the system. Also, the formation of a heterojunction with a Z-scheme mechanism and many surface reactive sites offered strong oxidative and reduction properties to the Bi_2WO_6/NH_2-UiO-66 composite, resulting in the

enhanced photoredox activity in the system. Furthermore, the strong interfacial interaction between NH_2-UiO-66 and Bi_2WO_6 established by the amine groups provided better stability to the Bi_2WO_6/NH_2-UiO-66 composite.

Conflicts of interest

The authors declare no conflict of interest.

Acknowledgements

> (i) References can be edited in the panel that appears to the right when you click on a reference.

1 T. aus der Beek, *et al.*, Pharmaceuticals in the environment—Global occurrences and perspectives, *Environ. Toxicol. Chem.*, 2016, **35**, 4, 823–835.

2 A. Küster and N. Adler, Pharmaceuticals in the environment: scientific evidence of risks and its regulation, *Philos. Trans. R. Soc. London, Ser. B*, 2014, **369**, 1656, 20130587.

3 S. K. Khetan and T. J. Collins, Human pharmaceuticals in the aquatic environment: a challenge to green chemistry, *Chem. Rev.*, 2007, **107**, 6, 2319–2364.

4 J. L. Martínez, Antibiotics and antibiotic resistance genes in natural environments, *Science*, 2008, **321**, 5887, 365–367.

5 M. E. de Kraker, A. J. Stewardson and S. Harbarth, Will 10 million people die a year due to antimicrobial resistance by 2050?, *PLoS Med.*, 2016, **13**, 11, e1002184.

6 C. Gadipelly, *et al.*, Pharmaceutical industry wastewater: review of the technologies for water treatment and reuse, *Ind. Eng. Chem. Res.*, 2014, **53**, 29, 11571–11592.

7 R. Anjali and S. Shanthakumar, Insights on the current status of occurrence and removal of antibiotics in wastewater by advanced oxidation processes, *J. Environ. Manage.*, 2019, **246**, 51–62.

8 M. B. Ahmed, *et al.*, Adsorptive removal of antibiotics from water and wastewater: progress and challenges, *Sci. Total Environ.*, 2015, **532**, 112–126.

9 V. Homem and L. Santos, Degradation and removal methods of antibiotics from aqueous matrices – a review, *J. Environ. Manage.*, 2011, **92**, 10, 2304–2347.

10 D. Li and W. Shi, Recent developments in visible-light photocatalytic degradation of antibiotics, *Chin. J. Catal.*, 2016, **37**, 6, 792–799.

11 A. Majumdar and A. Pal, Recent advancements in visible-light-assisted photocatalytic removal of aqueous pharmaceutical pollutants, *Clean Technol. Environ. Policy*, 2020, **22**, 1, 11–42.

12 K. Rokesh, M. Sakar and T.-O. Do, Emerging Hybrid Nanocomposite Photocatalysts for the Degradation of Antibiotics: Insights into Their Designs and Mechanisms, *Nanomaterials*, 2021, **11**, 3, 572.

13 M. J. Calvete, *et al.*, Hybrid materials for heterogeneous photocatalytic degradation of antibiotics, *Coord. Chem. Rev.*, 2019, **395**, 63–85.

14 X. Yang, *et al.*, Recent advances in photodegradation of antibiotic residues in water, *Chem. Eng. J.*, 2020, 126806.

15 A. Kaur and S. K. Kansal, Bi_2WO_6 nanocuboids: an efficient visible light active photocatalyst for the degradation of levofloxacin drug in aqueous phase, *Chem. Eng. J.*, 2016, **302**, 194–203.

16 J. Di, *et al.*, Reactable ionic liquid-assisted rapid synthesis of BiOI hollow microspheres at room temperature with enhanced photocatalytic activity, *J. Mater. Chem. A*, 2014, **2**, 38, 15864–15874.

17 J. Sun, *et al.*, Ultrasound-assisted synthesis of a feathery-shaped BiOCl with abundant oxygen vacancies and efficient visible-light photoactivity, *New J. Chem.*, 2018, **42**, 24, 19571–19577.

18 X. Zhang, *et al.*, Degradation of ciprofloxacin in aqueous bismuth oxybromide (BiOBr) suspensions under visible light irradiation: A direct hole oxidation pathway, *Chem. Eng. J.*, 2015, **274**, 290–297.

19 X. Xu, *et al.*, Oxygen vacancy boosted photocatalytic decomposition of ciprofloxacin over Bi_2MoO_6: Oxygen vacancy engineering, biotoxicity evaluation and mechanism study, *J. Hazard. Mater.*, 2019, **364**, 691–699.

20 M. Shang, W. Wang and H. Xu, New Bi_2WO_6 nanocages with high visible-light-driven photocatalytic activities prepared in refluxing EG, *Cryst. Growth Des.*, 2009, **9**, 2, 991–996.

21 T. Saison, *et al.*, New insights into Bi_2WO_6 properties as a visible-light photocatalyst. The, *J. Phys. Chem. C*, 2013, **117**, 44, 22656–22666.

22 H. Lv, *et al.*, Ionic liquid-assisted hydrothermal synthesis of Bi_2WO_6 – reduced graphene oxide composites with enhanced photocatalytic activity, *RSC Adv.*, 2014, **4**, 108, 63238–63245.

23 J. Zhang, *et al.*, Hierarchical Bi_2WO_6 architectures decorated with Pd nanoparticles for enhanced visible-light-driven photocatalytic activities, *Appl. Surf. Sci.*, 2017, **404**, 282–290.

24 J. Hu, *et al.*, Z-Scheme 2D/2D heterojunction of black phosphorus/monolayer Bi_2WO_6 nanosheets with enhanced photocatalyticactivities, *Angew. Chem., Int. Ed.*, 2019, **58**, 7, 2073–2077.

25 J. Bai, *et al.*, Oxygen Vacancy-Enhanced Ultrathin Bi_2O_3–Bi_2WO_6 Nanosheets' Photocatalytic Performances under Visible Light Irradiation, *Langmuir*, 2021, **37**, 16, 5049–5058.

26 S. Yin, *et al.*, Construction of NH_2-MIL-125 (Ti)/Bi_2WO_6 composites with accelerated charge separation for degradation of organic contaminants under visible light irradiation, *Green Energy Environ.*, 2020, **5**, 2, 203–213.

27 Q. Li, *et al.*, Rational design of MIL-88A(Fe)/Bi_2WO_6 heterojunctions as an efficient photocatalyst for organic pollutant degradation under visible light irradiation, *Opt. Mater.*, 2021, **118**, 111260.

28 Q. Wang and D. Astruc, State of the art and prospects in metal–organic framework (MOF)-based and MOF-derived nanocatalysis, *Chem. Rev.*, 2020, **120**, 2, 1438–1511.

29 J. Wu, *et al.*, Well-Designed TiO_2@UiO-66-NH_2 Nanocomposite with Superior Photocatalytic Activity for Tetracycline under Restricted Space, *Energy Fuels*, 2020, **34**, 10, 12911–12917.

30 S. Subudhi, *et al.*, UiO-66-NH$_2$ metal–organic frameworks with embedded MoS$_2$ nanoflakes for visible-light-mediated H$_2$ and O$_2$ evolution, *Inorg. Chem.*, 2020, **59**, 14, 9824–9837.

31 X. Zhang, *et al.*, g-C$_3$N$_4$/UiO-66 nanohybrids with enhanced photocatalytic activities for the oxidation of dye under visible light irradiation, *Mater. Res. Bull.*, 2018, **99**, 349–358.

32 J. Ding, *et al.*, UiO-66 (Zr) coupled with Bi$_2$MoO$_6$ as photocatalyst for visible-light promoted dye degradation, *J. Colloid Interface Sci.*, 2017, **497**, 126–133.

33 Y. Wang, *et al.*, Amino-Assisted NH$_2$-UiO-66 Anchored on Porous g-C$_3$N$_4$ for Enhanced Visible-Light-Driven CO$_2$ Reduction, *ACS Appl. Mater. Interfaces*, 2019, **11**, 34, 30673–30681.

34 K. Rokesh, M. Sakar and T.-O. Do, Calcium bismuthate (CaBiO$_3$): A potential sunlight-driven perovskite photocatalyst for the degradation of emerging pharmaceutical contaminants, *ChemPhotoChem*, 2020, **4**, 5, 373–380.

35 J. Wu, *et al.*, Well-Designed TiO$_2$@UiO-66-NH$_2$ Nanocomposite with Superior Photocatalytic Activity for Tetracycline under Restricted Space, *Energy Fuels*, 2020, **34**, 10, 12911–12917.

36 S. Sun, *et al.*, Ultrathin {001}-Oriented Bismuth Tungsten Oxide Nanosheets as Highly Efficient Photocatalysts, *ChemSusChem*, 2013, **6**, 10, 1873–1877.

37 L. Liang, *et al.*, Single unit cell bismuth tungstate layers realizing robust solar CO$_2$ reduction to methanol, *Angew. Chem., Int. Ed.*, 2015, **54**, 47, 13971–13974.

38 X. Zhang, *et al.*, Preparation and mechanism investigation of Bi$_2$WO$_6$/UiO-66-NH$_2$ Z-scheme heterojunction with enhanced visible light catalytic activity, *Inorg. Chem. Commun.*, 2020, **120**, 108162.

39 L. Liu, *et al.*, Dramatic activity of a Bi$_2$WO$_6$@gC$_3$N$_4$ photocatalyst with a core@shell structure, *RSC Adv.*, 2015, **5**, 120, 99339–99346.

40 T. Yang, *et al.*, A self-supporting UiO-66 photocatalyst with Pd nanoparticles for efficient degradation of tetracycline, *Appl. Surf. Sci.*, 2021, **544**, 148928.

41 S. Safa, *et al.*, Graphene quantum dots incorporated UiO-66-NH$_2$ as a promising photocatalyst for degradation of long-chain oleic acid, *Chem. Phys. Lett.*, 2021, **762**, 138129.

42 A. Crake, *et al.*, CO$_2$ capture and photocatalytic reduction using bifunctional TiO$_2$/MOF nanocomposites under UV-vis irradiation, *Appl. Catal., B*, 2017, **210**, 131–140.

43 M. Qamar, *et al.*, Highly efficient and selective oxidation of aromatic alcohols photocatalyzed by nanoporous hierarchical Pt/Bi$_2$WO$_6$ in organic solvent-free environment, *ACS Appl. Mater. Interfaces*, 2015, **7**, 2, 1257–1269.

44 S.-Q. Wang, *et al.*, Cu$_2$O@Cu@UiO-66-NH$_2$ Ternary Nanocubes for Photocatalytic CO$_2$ Reduction, *ACS Appl. Nano Mater.*, 2020, **3**, 10, 10437–10445.

45 J. Meng, *et al.*, Z-scheme photocatalytic CO$_2$ reduction on a heterostructure of oxygen-defective ZnO/reduced graphene oxide/UiO-66-NH$_2$ under visible light, *ACS Appl. Mater. Interfaces*, 2019, **11**, 1, 550–562.

46

Q. Hu, *et al.*, Construction of NH_2-UiO-66/BiOBr composites with boosted photocatalytic activity for the removal of contaminants, *Colloids Surf., A*, 2019, **579**, 123625.

47 J. Meng, *et al.*, Z-Scheme Photocatalytic CO_2 Reduction on a Heterostructure of Oxygen-Defective ZnO/Reduced Graphene Oxide/UiO-66-NH_2 under Visible Light, *ACS Appl. Mater. Interfaces*, 2019, **11**, 1, 550–562.

48 J. Li, *et al.*, Fast electron transfer and enhanced visible light photocatalytic activity using multi-dimensional components of carbon quantum dots@3D daisy-like In_2S_3/single-wall carbon nanotubes, *Appl. Catal., B*, 2017, **204**, 224–238.

49 B. Shao, *et al.*, Nitrogen-Doped Hollow Mesoporous Carbon Spheres Modified g-C_3N_4/Bi_2O_3 Direct Dual Semiconductor Photocatalytic System with Enhanced Antibiotics Degradation under Visible Light, *ACS Sustainable Chem. Eng.*, 2018, **6**, 12, 16424–16436.

50 C.-N. Ri, *et al.*, Construction of the Bi_2WO_6/$Bi_4V_2O_{11}$ heterojunction for highly efficient visible-light-driven photocatalytic reduction of Cr(VI), *New J. Chem.*, 2018, **42**, 1, 647–653.

51 M. B. Hussain, *et al.*, BiOCl-Coated UiO-66-NH_2 Metal–Organic Framework Nanoparticles for Visible-Light Photocatalytic Cr(VI) Reduction, *ACS Appl. Nano Mater.*, 2021, **4**, 4, 4037–4047.

52 B. Li, *et al.*, Facile hydrothermal synthesis of Z-scheme $Bi_2Fe_4O_9$/Bi_2WO_6 heterojunction photocatalyst with enhanced visible light photocatalytic activity, *ACS Appl. Mater. Interfaces*, 2018, **10**, 22, 18824–18836.

53 C. Zhao, *et al.*, Construction of direct Z-scheme Bi_5O_7I/UiO-66-NH_2 heterojunction photocatalysts for enhanced degradation of ciprofloxacin: Mechanism insight, pathway analysis and toxicity evaluation, *J. Hazard. Mater.*, 2021, 126466.

54 X. Wei, *et al.*, The Z-scheme NH_2-UiO-66/PTCDA composite for enhanced photocatalytic Cr(VI) reduction under low-power LED visible light, *Chemosphere*, 2021, **280**, 130734.

Footnotes

[†] Electronic supplementary information (ESI) available. See DOI: 10.1039/d1nj03977f

Queries and Answers

Q1

Query: Funder details have been incorporated in the funder table using information provided in the article text. Please check that the funder information in the table is correct.

Answer: Yes, It's correct.